Non-Hertzian Stress Fields in Simulated Porous Sandstone Grains and Implications for Compactive Brittle Failure
A High-Resolution FEM Approach

Shinohara, Takahiro; Thieulot, Cedric; Spiers, Christopher J.; Hangx, Suzanne J.T.

Correspondence to:

T. Shinohara,
t.shinohara@tudelft.nl

Non-Hertzian Stress Fields in Simulated Porous Sandstone Grains and Implications for Compactive Brittle Failure—A High-Resolution FEM Approach

Takahiro Shinohara[1,2] [ID], **Cedric Thieulot[1]** [ID], **Christopher J. Spiers[1]** [ID], and **Suzanne J. T. Hangx[1]** [ID]

[1]Department of Earth Sciences, Utrecht University, Utrecht, The Netherlands, [2]Now at Department of Geoscience and Engineering, Delft University of Technology, Delft, The Netherlands

Abstract Fluid extraction from sandstone reservoirs leads to reservoir compaction, potentially inducing surface subsidence and seismicity, as observed in the Groningen Gas Field, Netherlands. Such compaction is partly elastic, but can additionally be caused by instantaneous plastic and rate/time-dependent processes, such as subcritical crack growth, meaning that compaction may continue even if production is stopped. Despite the need to evaluate the impact of post-abandonment reservoir behavior (>10–100 years), few mechanism-based, rate/time-dependent compaction laws exist. Compaction due to grain breakage, either via critical or subcritical crack growth, is driven by tensile stresses acting on surface and volume flaws. We performed high-resolution 3D linear elastic finite element method simulations on simplified grain assemblies to investigate the effect of stress–strain boundary conditions, porosity and mineralogical variations on grain-scale stress fields. Our simulations showed tensile stress concentrations at grain contact edges and on pore walls, which increased in magnitude with increasing aggregate porosity and local porosity variation. The fraction of surface area with tensile stresses sufficient to extend flaws with a size up to 30 μm showed a clear correlation with compactive yield envelopes for the Groningen reservoir sandstone. This suggests that compactive failure is related to the probability of pre-existing surface flaws, falling in a pore surface region where the Griffith criterion is satisfied. A preliminary, time-independent failure probability model, using the observed tensile stress distribution, qualitatively predicts a non-linear increase in grain cracking during deviatoric loading, and suggests a new route to predict sandstone compaction through brittle grain failure.

Plain Language Summary Activity underground, such as gas extraction from sandstone reservoirs, compacts the sandstone and sometimes causes surface subsidence and earthquakes, as in the Groningen Gas Field, Netherlands. Compaction partly occurs in a slow, permanent manner, caused by processes such as time-dependent, chemically-enhanced cracking of the sandstone grains. This means that compaction, and any subsidence or earthquakes, may continue even if gas extraction is stopped. Slow grain cracking is driven by tensile stresses acting on pre-existing microcracks on grain surfaces. We conducted numerical simulations on sandstone-like grain assemblies, calculating the stress distribution on grain (pore wall) surfaces. The results indicate that sandstone compaction by grain cracking is related to this distribution. Employing this observation, we developed a preliminary model, which qualitatively predicts grain cracking behavior observed in sandstones. This is a first step toward a model for slow sandstone compaction due to chemically-enhanced slow cracking, and toward prediction of surface subsidence and earthquakes associated with exploitation of sandstone reservoirs.

1. Introduction

Hydrocarbon extraction and geothermal heat production from sandstone reservoirs frequently result in surface subsidence and are occasionally accompanied by induced seismicity (Davies et al., 2013; Eberhart-Phillips & Oppenheimer, 1984; Fialko & Simons, 2000; Hettema et al., 2002; Morton et al., 2001; Mossop & Segall, 1997; Suckale, 2009; Van Wees et al., 2014). Subsidence occurs as a result of reservoir compaction at depth, caused by the increase in effective stress due to pore pressure reduction and/or thermal contraction due to cooling. The magnitude of subsidence can amount to several tens of centimeters, which for typical reservoir thicknesses of the order of 50–100 m corresponds to a vertical reservoir strain of <0.5% (Morton et al., 2001; Mossop & Segall, 1997; Van Thienen-Visser & Breunese, 2015). Reservoir compaction is often assumed to be purely poroelastic (Bourne & Oates, 2020; Dempsey & Suckale, 2017; Zbinden et al., 2017), meaning it is linear,

Writing – original draft:
Takahiro Shinohara
Writing – review & editing:
Takahiro Shinohara, Cedric Thieulot,
Christopher J. Spiers, Suzanne J. T. Hangx

reversible, rate-insensitive and easily quantified (Wang, 2000). However, when grain contact and grain volume stresses become too high, grain-scale deformation may lead to permanent, inelastic compaction. Both field data (Santarelli et al., 1998) and experimental studies (Bernabé et al., 1994; Hol et al., 2015, 2018; Pijnenburg et al., 2018, 2019a, 2019b; Shalev et al., 2014) of highly porous sandstones have shown that a significant part of the accumulated deformation is permanent even at small strains. The grain-scale mechanisms causing this inelastic deformation are still poorly understood, as is the potential rate-sensitivity of such mechanisms (Spiers et al., 2017; Van Thienen-Visser & Breunese, 2015; Van Wees et al., 2018). On production timescales (i.e., several decades) and at stresses and strains relevant to depleting hydrocarbon reservoirs, recent studies suggest that inelastic deformation in sandstones containing intergranular clay films is largely accommodated by virtually time- or rate-insensitive compaction of and sliding along these clay films (Pijnenburg et al., 2019b; Verberne et al., 2021). In other sandstones, grain rearrangement is the dominant inelastic deformation mechanism (Shalev et al., 2014). However, field evidence suggests that compaction may continue even after production stops (Mallman & Zoback, 2007), implying a role of time-dependent mechanisms in reservoir compaction (Brantut et al., 2014; Heap et al., 2015; Pijnenburg et al., 2018; Stanchits et al., 2009; De Waal & Smits, 1988). Therefore, to predict the long-term impact of production strategies more reliably, identifying and quantifying the grain-scale mechanisms leading to compaction is key. This issue is particularly critical for the seismogenic Groningen Gas Field located in the densely populated north of the Netherlands, where production from the Slochteren sandstone reservoir has led to surface subsidence and widespread induced seismicity. To halt these phenomena, production from the Slochteren reservoir was permanently ended on 19 April 2024 (Ministry of Economic Affairs and Climate Policy, 2024). However, the extent and duration of future time-dependent compaction and associated seismicity, now that production has stopped, remain uncertain.

One of the possible mechanisms controlling rate-sensitive inelastic deformation in upper crustal, quartz-rich sandstone reservoirs is grain breakage, either via critical or subcritical cracking (Brantut et al., 2013, 2014; Heap et al., 2009a, 2009b, 2015; Pijnenburg et al., 2018). Crack growth is driven by grain contact and grain volume tensile stresses σ_T acting on surface and volume flaws. It is therefore key to quantify the grain contact and grain body tensile stress fields driving the crack growth that could potentially govern inelastic reservoir compaction.

Grain contact and/or grain body stress fields have been explored experimentally through the use of stressed photo-elastic Plexiglas spheres, discs and/or simulated grains (Hiramatsu & Oka, 1966), as well as using state-of-the-art techniques combining synchrotron X-ray computed tomography with three-dimensional X-ray diffraction on granular materials (Hurley et al., 2016, 2018; Zhai et al., 2020). However, quantification of the stress fields at the grain contact-scale (i.e., in the order of microns to sub-microns) within (rock) materials has remained challenging. Spherical grain contact stresses have been quantified analytically, following Hertzian contact theory (Hertz, 1881). Hertzian contact theory, combined with linear elastic fracture mechanics (LEFM), is able to reasonably accurately predict the hydrostatic crushing pressure of porous rocks, assuming a spherical grain aggregate where initial flaw size scales with grain size (Zhang et al., 1990). This model has also been extended to consider the effect of differential stress (Guéguen & Fortin, 2013).

Unfortunately, however, the Hertzian approach neglects the fact that grains in sandstones are not perfect spheres in point contact. Instead grain contacts are indented, sutured and/or cemented (McBride, 1989). Therefore, they will likely behave in a non-Hertzian manner characterized by sub-Hertzian stress concentrations. This complexity increases resistance to the propagation of flaws and ultimately grain-scale fracturing (Bernabé et al., 1992; Sackfield & Hills, 1986). Furthermore, Hertzian contact theory predicts that cracking initiates from small pre-existing flaws at the edge of the grain contact region, where the highest tensile stress is expected (Zhang et al., 1990). However, experimental work has shown that in natural sands and sandstones, pits, grooves and scratches of up to tens of micrometers in depth exist on grain surfaces, outside of the contact area (e.g., Brzesowsky et al., 2011; Pijnenburg et al., 2019a; Pijnenburg & Spiers, 2020). Given their substantial flaw size, it is possible that cracking is initiated at this type of defect (Brzesowsky et al., 2011). In addition, rather than a grain size-dependent initial flaw size, for which there is no clear physical basis, it is possible that surface roughness, or grain size-dependent asperity size, plays a role in controlling grain breakage, as well as flaws, asperities and other stress concentrators within indented or truncated grain contact zones. Lastly, grain-scale heterogeneity may also play an important role in the stress magnitude and/or distribution, which is often neglected.

High-resolution finite element method (FEM) computations offer one of the most promising ways to quantify contact and pore wall stresses (e.g., Imseeh & Alshibli, 2018; Turner et al., 2016; Wong & Wu, 1995). Though FEM offers a way to calculate grain-contact and whole-grain stress and strain fields for an irregular array of grains, and would allow a systematic study of the effect of natural textural variability, few studies have done so taking into account realistic stress or strain boundary conditions. Stress fields in calcite-cemented quartz grains have been quantified via 2D axisymmetric FEM at a mesh resolution down to ~ 1 μm (Wong & Wu, 1995), and show that cementation significantly reduces the tensile stress at the grain contact edge. Recently, 3D FEM simulations have been conducted to calculate the grain-scale stress and strain fields in quartz-rich sand aggregates containing tens to hundreds of grains (Imseeh & Alshibli, 2018; Turner et al., 2016), though mesh resolutions were restricted to ~ 20 μm due to high computational cost. While such 3D simulations of realistic sand packs (Imseeh & Alshibli, 2018) have been able to replicate behavior seen in experiments, the limitations of the mesh resolution prevented inferences on the detailed stress distribution at the grain contacts and pore walls.

In this study, we performed high-resolution (i.e., $\sim$ micron-sized mesh), 3D linear elastic FEM simulations on simplified assemblies consisting of grains of quartz and/or feldspar, with or without intergranular clay films. Grain contacts were approximated as flattened interfaces between grains. We systematically investigated the effect of stress boundary conditions, packing geometry, porosity and mineralogical variations on the minimum principal stress $\tilde{\sigma}_3$ fields developed at grain contacts, pore walls and throughout grain volumes. We discuss the relative importance of those factors, and how the observed tensile stress distributions may drive the initiation of critical (i.e., equilibrium) crack growth leading to time-independent grain deformation. Finally, a new route to develop grain cracking models, either via critical or subcritical cracking, is suggested, with the aim of more reliably predicting the long-term impact of fluid extraction on sandstone reservoir compaction, in particular, in the context of the Groningen Gas Field.

2. Finite Element Model of Grain Clusters

Upper crustal sandstones are typically composed of quartz, with lesser amounts of feldspar, clays and other minerals, such as carbonates (e.g., Heap et al., 2009b; Klein et al., 2001; Ngwenya et al., 2001). In this study, we simulated quartz-rich, unconsolidated or poorly cemented sandstone with subordinate feldspar (albite) grains and thin intergranular clay films (kaolinite), representative for a range of porous sandstones (e.g., Heap et al., 2009b; Klein et al., 2001; Ngwenya et al., 2001; Pijnenburg et al., 2019b). We employed values for Young's modulus E and Poisson's ratio ν of 95 GPa and 0.08 for quartz (Zhang et al., 1990), and 89 GPa and 0.247 for feldspar (i.e., albite) (Brown et al., 2016), respectively (see Table 1 for symbols and units).

We explored two different grain packing geometries; cubic packing and hexagonal packing (Figure 1). To simplify the sandstone microstructure for our simulations, keeping the computational cost low, we represented grains as spherical bodies truncated at planar grain contacts, yet departing slightly and continuously from this plano-spherical geometry to facilitate convergence of FEM-solutions in contact margin regions. Given the complexity of such simulations and the symmetry of the selected packing geometries, we focused on grain clusters consisting of up to three (partial) grains. Accordingly, this approach is only applicable to conditions where negligible strain localization/heterogeneity occurs (i.e., before macroscopic failure). In addition, the model is limited to application to relatively homogeneous sandstone in terms of grain size.

The grain bodies behave linear-elastically, and frictional sliding is allowed between grain contacts (Figure 1). The grains have an average grain radius R of 100 μm (i.e., 200 μm grain size). We systematically varied the aggregate porosity from 12.0% to 29.0% by changing the radius of the grain contact a for each packing geometry (cf. Figures 1a and 1b). This porosity range covers most porous sandstones (e.g., Pijnenburg et al., 2018; Zhang et al., 1990). In addition, observations in natural porous sandstones suggest that porosity could be locally higher/ lower than the average porosity (Baud et al., 2015). Therefore, we also explored the effect of local porosity variations on the development of stress concentration. To achieve this, we developed aggregates consisting of two grains with different diameters and contact radius (Figure 1c). In this specific case, we defined the ratio of the radius of the flat grain contact of the "irregular" grain (a_{ir}) to the radius of the flat contact of the reference grains (a—see Figure 1c). For the cubic pack, we employed a grain contact radius ratio a_{ir}/a of 0.3, corresponding to a local porosity ϕ_{local} of 38.5% and 42.9% for aggregate porosities of 12% and 29%, respectively. Note that the local porosity was calculated for a domain bounded by a cube with a side length of $2d$, fixed around the center of the "irregular grain" (Figure 1c). The effect of introducing a feldspar grain into a given irregular pack was

Table 1
Nomenclature of the Parameters Used in the Finite Element Method Models

Symbol	Meaning
a	Grain contact radius [m]
a_{ir}/a	Contact radius ratio [−]
E	Young's modulus [Pa]
K	Bulk modulus [Pa]
P	Mean stress $((\sigma_1 + \sigma_2 + \sigma_3)/3)$ [Pa]
Q	Differential stress $(\sigma_1 - \sigma_3)$ [Pa]
R	Grain radius [m]
ε_1	Externally-applied axial strain [−]
ε_2	Externally-applied lateral strain [−]
ε_3	Externally-applied lateral strain [−]
μ	Friction coefficient [−]
ν	Poisson's ratio [−]
$\tilde{\sigma}_T$	Local tensile stress [Pa]
$\tilde{\sigma}_T^{max.}$	Local maximum tensile stress [Pa]
σ_1	Maximum principal stress [Pa]
σ_2	Intermediate principal stress [Pa]
σ_3	Minimum principal stress [Pa]
$\tilde{\sigma}_1$	Local maximum principal stress [Pa]
$\tilde{\sigma}_3$	Local minimum principal stress [Pa]
ϕ_{local}	Local porosity [−]
ϕ	aggregate porosity [−]

investigated by replacing the smaller quartz grain with a feldspar grain. To simulate grain contacts containing intergranular clay films, the intergranular friction coefficient μ was set to 0.28 (Pijnenburg et al., 2018), while it was set to 0.6 for quartz-quartz or quartz-feldspar contacts (estimated from e.g., Chester, 1994). The resulting aggregates were converted to a finite element tetrahedral mesh using ABAQUS/Standard (Smith, 2009). A mesh size grading from 2 μm at the grain surface to 6 μm at the core of the grain body was employed to ensure that the computed stresses are independent of mesh size (Figure 1d). Around grain contact edges, mesh structure was found to significantly affect the computed stresses. We therefore employed a semi-structured mesh geometry around the grain contact edges, so as to minimize the dependence of our results on the mesh structure. The depicted mesh in Figure 1d is the result of extensive testing and consists of up to 1.4 million mesh elements in each aggregate simulation.

Using ABAQUS/Standard (Smith, 2009), we performed two types of compression simulations on our sandstone aggregates: (a) hydrostatic compression and (b) triaxial compression. Note that we adopt the convention that compressive stresses, as well as compressive strains and displacements, are measured positive in this paper. The principal compressive stresses are denoted as $\sigma_1 \geq \sigma_2 = \sigma_3$. Both simulation types were aimed at systematically investigating the effect of porosity and mineralogy, and local porosity variations therein, on the resulting stress fields within the individual grains. While the cubic packing geometry was only compressed under a hydrostatic stress (i.e., $\sigma_1 = \sigma_2 = \sigma_3$), the hexagonal packing geometry was compressed under both hydrostatic and triaxial stresses to investigate the effect of non-hydrostatic (i.e., $\sigma_1 > \sigma_2 = \sigma_3$) loading on local stress concentrations within the grains and grain surfaces (i.e., grain contacts and pore walls). In all simulations, we imposed a displacement boundary condition (i.e., Dirichlet boundary condition) on the six sides of the domain to generate the internal grain stress fields. For homogeneous clusters (Figures 1a and 1b), that is without any mineralogical or porosity variations, a displacement boundary condition was applied such that the desired macroscopic stress, calculated by dividing the total normal force applied to a cluster boundary by its area, was satisfied at each boundary. For the hydrostatic compression simulations, using the cubic packing geometry, equal displacements were applied to all the three grain contacts and hence cluster walls (i.e., $D_1 = D_2 = D_3 > 0$) using rigid walls (Figure 1a), resulting in a final hydrostatic compressive strain (i.e., $\varepsilon_1 + \varepsilon_2 + \varepsilon_3$ where $\varepsilon_1 = \varepsilon_2 = \varepsilon_3$) of up to 0.33%–0.66% achieved at a mean stress $P \left(= \frac{1}{3}(\sigma_1 + \sigma_2 + \sigma_3)\right)$ of 63 MPa. Due to the symmetric nature of the assemblies, the normal displacement of the other surfaces (i.e., bottom, left and front) was set to zero. For the hydrostatic compression simulations using the hexagonal packing geometry, the appropriate, non-equal displacements were searched and applied to the three (i.e., top, right and front) cluster boundaries, resulting in a final hydrostatic compressive strain (i.e., $\varepsilon_1 + \varepsilon_2 + \varepsilon_3$) of up to 0.55% at $P = \sigma_1 = \sigma_2 = \sigma_3 = 42$ MPa. In the triaxial compression simulations, the top horizontal boundary was subjected to a larger displacement than the vertical boundaries (right and front), corresponding to axial (ε_1) and horizontal ($\varepsilon_2 = \varepsilon_3$) strains of up to 0.7% and 0.3%, respectively. As in the hydrostatic simulations, the normal displacement of the other surfaces (i.e., bottom, left and back) was set to zero. For heterogeneous clusters, that is the aggregates consisting of two grains with different diameters and relative contact radius (Figure 1c), a polynomial function was employed to describe the appropriate displacement boundary conditions. These functions were obtained from a larger-scale (∼10 grains), in-house linear-elastic 2D model, which enabled us to relate the applied displacement to macroscopic stress in our 3D simulations (see Text S1 and S2 in Supporting Information S1).

All simulations are summarized in Table 2. Note that the values of the local minimum principal compressive stress $\tilde{\sigma}_3^{min}$, ε_1 and ε_3 presented are those at a mean stress P of 63 and 42 MPa for cubic and hexagonal packings, respectively.
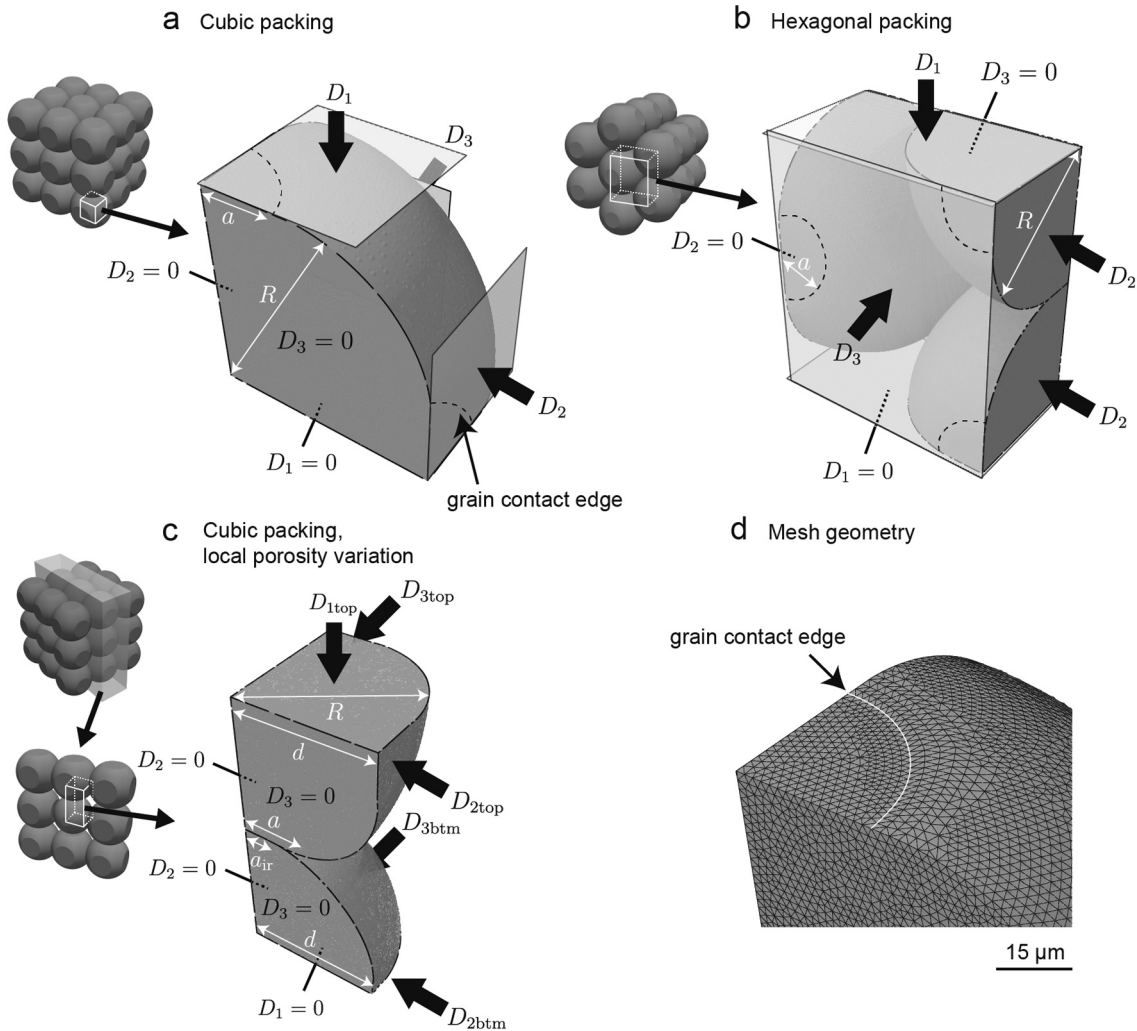
Figure 1. Selected 3D grain clusters. (a) A 1/8th of a quartz grain with radius R and contact radius a and indicated loading geometry, corresponding to a portion of a cubic pack. (b) Hexagonal packing of grains and indicated loading geometry. (c) A cubic packing configuration including a local porosity variation, with the bottom grain having a smaller contact radius a ($a_{ir}/a = 0.3$). (d) Close-up of the tetrahedral mesh near the grain contact with a resolution of about 2 μm.

3. Results

We will first show results obtained for triaxial compression since this treats homogeneous, hexagonally packed grain clusters. We will then go on to show results obtained from hydrostatic compression since this partly treats heterogeneous, cubic packed grain clusters.

3.1. Triaxial Compression of Hexagonally Packed Homogeneous Grain Clusters

Minimum principal stress $\tilde{\sigma}_3$ fields for representative grain clusters compressed to develop a mean stress P $\left(=\frac{1}{3}(\sigma_1 + \sigma_2 + \sigma_3)\right)$ of 42 MPa are presented in Figure 2 (i.e., hx-series of simulations, Table 2). Note that the imposed deformation and resulting stress paths have negligible effect on the tensile stress development in our simulations (see Text S3 in Supporting Information S1), hence the maximum tensile stress $\tilde{\sigma}_T^{max.}$ (i.e., the magnitude of min. $\tilde{\sigma}_3$) is just a function of mean stress and differential stress. In all simulations, zones of tensile stresses (i.e., $\tilde{\sigma}_3 < 0$) can be observed not just at the edge of the grain contact, but also along substantial sections of the pore wall (e.g., Figures 2a–2c) and within the grain bodies (Figure 2). Overall, the tensile magnitude of the minimum principal stress $\tilde{\sigma}_3$ increases with increasing porosity. At a vertical stress (i.e., σ_1) of 65 MPa and horizontal stresses (i.e., $\sigma_2 = \sigma_3$) of 30 MPa, the maximum tensile stress $\tilde{\sigma}_T^{max.}$ value (the magnitude of min. $\tilde{\sigma}_3$-value) at the periphery of the grain contact increases from 140 to 462 MPa as porosity increases from 12% to 26%

Table 2
Summary of an Finite Element Method Simulations, Including Key Input Parameters and Resulting Mechanical Data

Simulation	ϕ [%]	a [µm]	a_{ir}/a [−]	μ [−]	K [GPa]	min. $\tilde{\sigma}_3$ [MPa]	ε_1 [%]	ε_2 [%]	ε_3 [%]	σ_1 [MPa]	σ_2, σ_3 [MPa]
Hexagonal packing ($P \sim 42$ MPa)											
hx12	12.0	45.4	1	0.60	18.6	−91	0.08	0.05	0.11	47	40
						−91	0.09	0.04	0.09	53	36
						−140	0.08	0.02	0.04	65	30
						−173	0.19	0.01	0	90	18
hx18	18.0	36.9	1	0.60	13.8	−145	0.10	0.06	0.14	47	40
						−158	0.15	0.07	0.16	53	36
						−253	0.15	0.04	0.10	65	30
						−279	0.25	0.01	0	90	18
hx26	26.0	25.7	1	0.60	8.34	−258	0.15	0.13	0.27	42	42
						−276	0.16	0.10	0.24	47	40
						−286	0.23	0.12	0.27	53	36
						−462	0.24	0.07	0.17	65	30
						−551	0.39	0.04	0	90	18
hx26-μ0.28	26.0	25.7	1	0.28	8.34	−258	0.15	0.13	0.27	42	42
						−276	0.16	0.10	0.24	47	40
						−280	0.23	0.12	0.27	53	36
						−372	0.24	0.07	0.17	65	30
Cubic packing ($P \sim 63$ MPa)											
cb12	12.0	52.4	1	0.60	20.4	−95	0.11	0.11	0.11	63	63
cb18	18.0	45.1	1	0.60	15.6	−121	0.14	0.14	0.14	63	63
cb29	29.0	31.7	1	0.60	9.2	−179	0.22	0.22	0.22	63	63
cb12–0.3	12.0	52.4	0.3	0.60	n.a.	−165	n.a.	n.a.	n.a.	63	63
cb29–0.3	29.0	31.7	0.3	0.60	n.a.	−365	n.a.	n.a.	n.a.	63	63
cb29-0.3-μ0.28	29.0	31.7	0.3	0.28	n.a.	−360	n.a.	n.a.	n.a.	63	63
cb12-0.3-fsp	12.0	52.4	0.3	0.60	n.a.	−150	n.a.	n.a.	n.a.	63	63
cb29-0.3-fsp	29.0	31.7	0.3	0.60	n.a.	−298	n.a.	n.a.	n.a.	63	63

*Note.* The grain radius for all (partial) grains is 100 µm, except in those where $a_{ir}/a < 1$.

(Figures 2a–2c). Furthermore, imposing displacements that generate a differential stress upon the cluster (i.e., $\sigma_1 > \sigma_2 = \sigma_3$) leads to shear stress at grain contacts, though this is insufficient to activate full contact sliding in all simulations. While for purely normally loaded contacts, the tensile stress $\tilde{\sigma}_T$ (i.e., $\tilde{\sigma}_3 < 0$) develops uniformly around the periphery of the grain contact, inclined contacts undergoing shear show a non-uniform $\tilde{\sigma}_T$ stress distribution (e.g., Figures 2a–2c). For those contacts, the largest tensile stress $\tilde{\sigma}_T^{max.}$ (i.e., the magnitude of min. $\tilde{\sigma}_3$) is observed at the downward end of the contact of the overriding grain. Generating a differential stress increases the maximum tensile stress at these locations by a factor of 3 and increases the portion of the grain volume and pore area in tension, even for the same mean stress (compare Figures 2c and 2d). Simulating the presence of intergranular clay films, by decreasing the grain contact friction, shows negligible effect on the tensile stress distribution in the grain volume and along the pore wall away from the periphery of the grain contact for the stress conditions investigated (e.g., compare Figures 2c and 2e). However, the presence of intergranular clay films reduces the maximum tensile stress at the periphery of the grain contact, notably at higher differential stress (see Table 2). For example, under conditions where $\sigma_1 = 65$ MPa and $\sigma_2 = \sigma_3 = 30$ MPa, the largest tensile stress $\tilde{\sigma}_T^{max.}$ (i.e., the magnitude of min. $\tilde{\sigma}_3$) value decreases from 462 to 372 MPa in the presence of clay in the grain contact (19% reduction in maximum tensile stress).
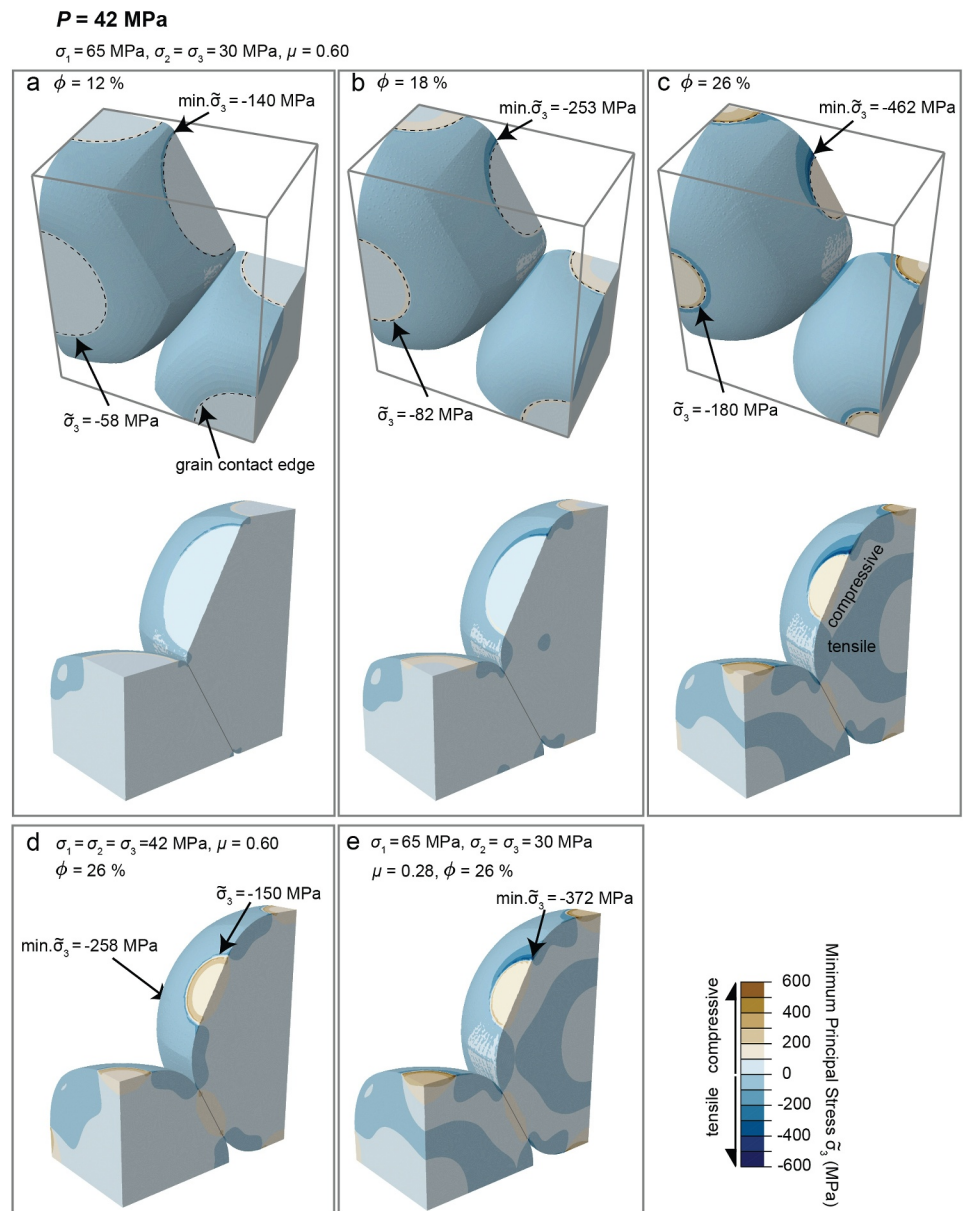
Figure 2. Minimum principal stress $\tilde{\sigma}_3$ fields for grain clusters consisting of three quartz grains of uniform grain size, with and without intergranular clay films, compressed at a mean stress of 42 MPa. Note that for visualization purposes the top 1/8th grain has been removed (cf. Figure 1b). Stress field on the grain surface and within grain bodies for a cluster compressed at an axial stress σ_1 of 65 MPa and a confining stress σ_3 of 30 MPa, for an aggregate porosity of (a) $\phi = 12\%$ (hx12), (b) $\phi = 18\%$ (hx18), and (c) $\phi = 26\%$ (hx26). (d) Stress field distribution for a clay-free ($\mu = 0.60$) cluster with $\phi = 26\%$ (hx26) under hydrostatic compression (i.e., $\sigma_1 = \sigma_2 = \sigma_3 = 42$ MPa). (e) Stress field distribution for a cluster containing intergranular clay films ($\mu = 0.28$) and a porosity of 26% compressed at $\sigma_1 = 65$ MPa and $\sigma_2 = \sigma_3 = 30$ MPa (hx26-μ0.28).

3.2. Hydrostatic Compression of Cubic Packed Grain Clusters: Effect of Heterogeneous Porosity and Mineralogy

Minimum principal stress $\tilde{\sigma}_3$ fields for representative grain clusters compressed to achieve a hydrostatic stress ($P = \sigma_1 = \sigma_2 = \sigma_3$) of 63 MPa are presented in Figure 3 (i.e., cb-series, Table 2). In all simulations, zones of tensile stress (i.e., $\tilde{\sigma}_3 < 0$) can be observed not just at the edge of the grain contact, but also along substantial sections of the pore wall and within grain bodies. Note the distinctly different grain body stress distributions compared to the hexagonally packed clusters (cf. Figures 2a–2c vs. Figures 3a–3c). As expected, the largest tensile stress $\tilde{\sigma}_T^{\text{max.}}$, or min. $\tilde{\sigma}_3$, is observed at the grain contact edges. Moreover, when $P = \sigma_1 = \sigma_2 = \sigma_3 = 63$ MPa,
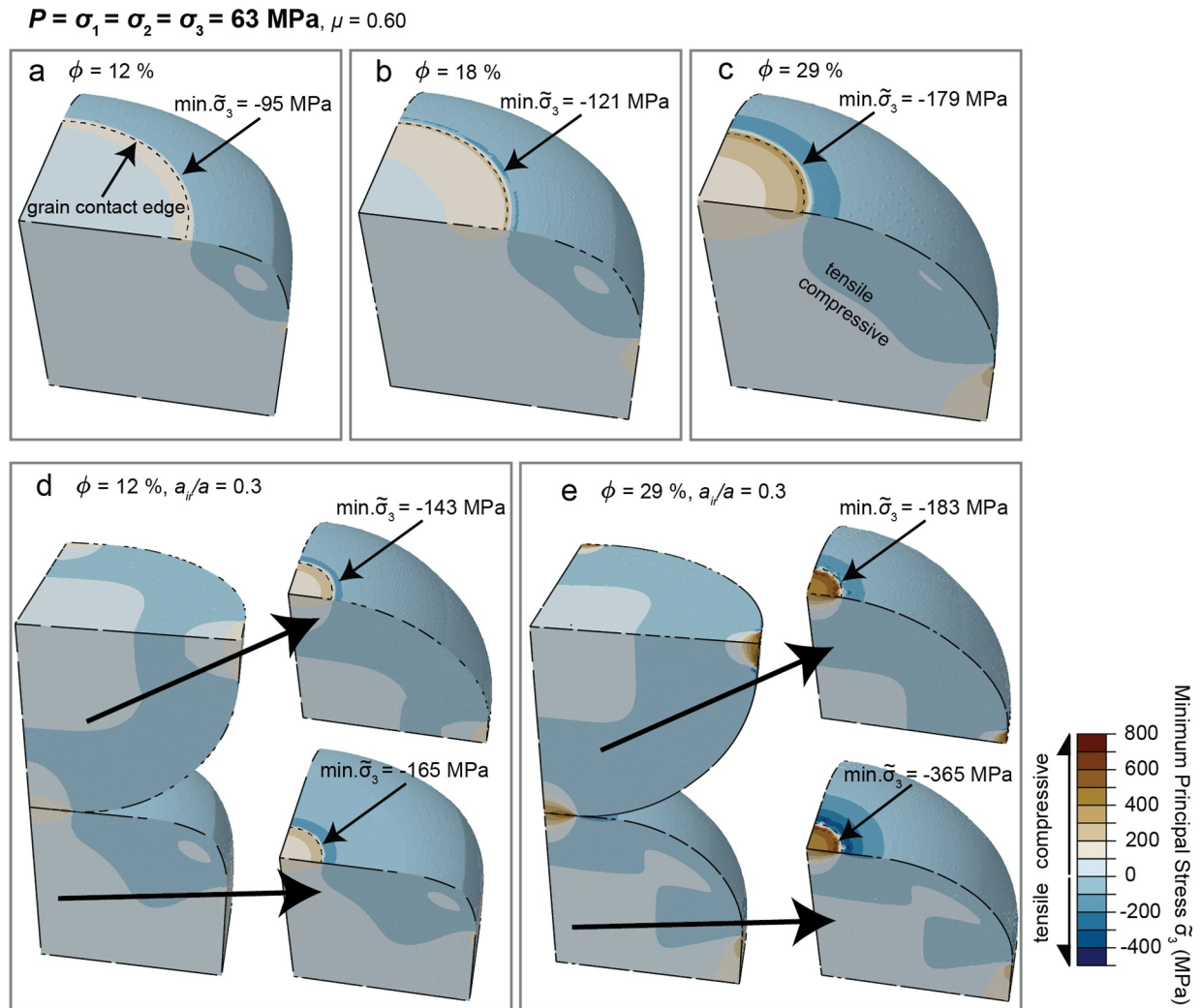
Figure 3. Minimum principal stress $\tilde{\sigma}_3$ fields for clay-free grain clusters consisting of two quartz grains compressed at a hydrostatic stress of 63 MPa. Stress distribution on the grain surface and within the grain body for a cluster with a uniform grain size and an aggregate porosity of (a) $\phi = 12\%$ (cb12), (b) $\phi = 18\%$ (cb18), and (c) $\phi = 29\%$ (cb29). Stress fields for a cluster consisting of a smaller (top) and larger (bottom) grain simulating local variations in porosity for (c) a ϕ_{local} of 38.5% (i.e., $a_{ir}/a = 0.3$, $\phi = 12\%$—cb12-0.3) and (d) a ϕ_{local} of 42.9% (i.e., $a_{ir}/a = 0.3$, $\phi = 29\%$—cb29-0.3).

the maximum tensile stress $\tilde{\sigma}_T^{max.}$ value (i.e., the magnitude of min. $\tilde{\sigma}_3$-value) at the periphery of the grain contact increases from 95 to 179 MPa as porosity increases from 18% to 29% (Figures 3a–3c). In contacts between grains with different grain sizes and contact areas, local porosity variations, caused by variations in grain size and contact area, lead to an increase in the maximum tensile stress $\tilde{\sigma}_T^{max.}$ (i.e., the magnitude of min. $\tilde{\sigma}_3$) value by a factor of roughly 2 from 95 to 165 MPa and from 179 to 365 MPa at $\phi = 12\%$ and $\phi = 29\%$, respectively (Figures 3d and 3e). By contrast, changes in the friction coefficient of grain contacts, simulating the presence or absence of a clay film, showed no significant effect on the minimum principal stress $\tilde{\sigma}_3$ fields (change in maximum tensile stress $\tilde{\sigma}_T^{max.} < 1.4\%$; Table 2). Locally replacing a quartz grain by a feldspar (i.e., albite) grain leads to a reduction in tensile stress magnitude. Overall, by replacing quartz with feldspar, a reduction in maximum tensile stress $\tilde{\sigma}_T^{max.}$ of 9% and 18% is observed in the quartz grain for clusters of 12% and 29% porosity, respectively (cf. min. $\tilde{\sigma}_3$ for cb12–0.3 vs. cb12-0.3-fsp, and cb29–0.3 vs. cb29-0.3-fsp; Table 2). Note that the tensile stress distribution is not significantly affected by replacing a quartz grain with a feldspar grain.

From the hydrostatic simulations, we were able to derive the cumulative frequency distribution of the tensile stress along the surface (i.e., pore wall and grain contact) of single grains (Figure 4). The cumulative frequency distribution is the area fraction along pore walls plus contacts, per cluster, having a tensile stress less than or equal
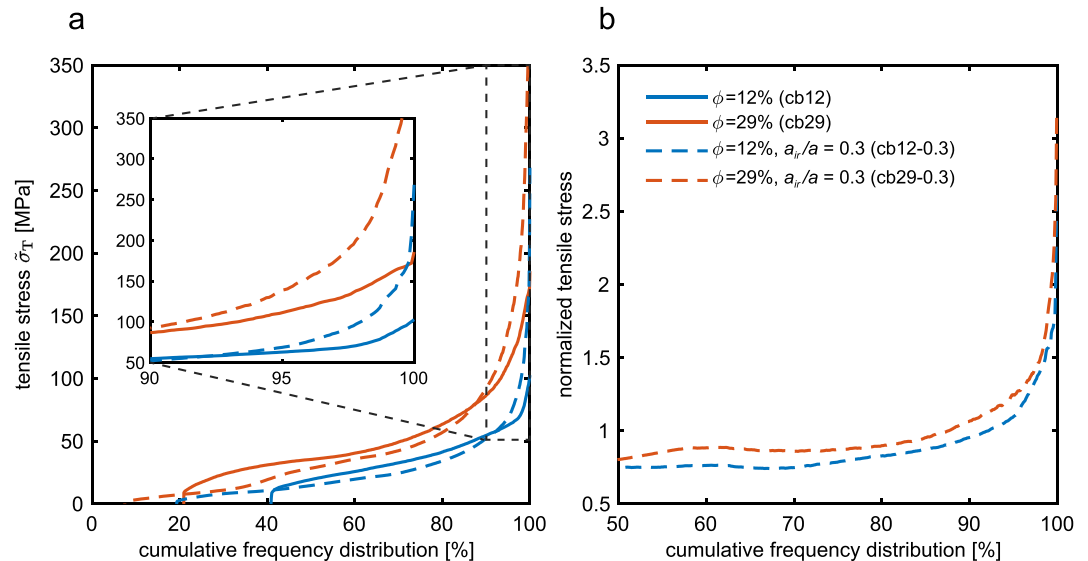
Figure 4. Cumulative frequency distribution of tensile stresses of magnitude σ_T ($=\sigma_3$) along the total surface of a grain in a cubic packed cluster. This is defined as the area fraction along pore walls plus contacts, per cluster, having a tensile stress less than or equal to the value plotted. (a) Cumulative distribution of tensile stress for regular and irregular packs of low (12%) and high (29%) porosity. (b) Normalized cumulative frequency distribution of tensile stress for the clusters with local porosity variation. Note that normalization was performed with respect to cumulative frequency distribution for homogeneous clusters of the same porosity, at given cumulative frequency distribution values.

to the value plotted. Overall, for the low porosity cluster (12% porosity), tensile stresses developed on 60% of the grain surface, of which 80% fell within the tensile range of 10–50 MPa (Figure 4a). By contrast, when porosity increases (29%), tensile stresses developed on 80% of the grain surface, of which 85% fell within the tensile range 10–80 MPa with maximum stresses of ∼180 MPa. Only when variations in local porosity are introduced do tensile stresses increase above 180 MPa. In general, local porosity increases intensify the magnitude of the top 10% of the tensile stress values attained by a factor of up to 2–3, while simultaneously the majority of the tensile stresses developed is reduced in magnitude by up to 20%–25%. Normalizing the tensile stress for the clusters with heterogeneous porosity with respect to that for homogeneous clusters of the same porosity, at given cumulative frequency distribution values (Figure 4b), demonstrates that this change in the tensile stress distribution is independent of ϕ.

4. Tensile Stress Magnitude and Distribution During Loading: Implications for Critical Crack Growth

Our simulations on compressed (partial) clusters of quartz grains, with and without intergranular clay films, have shown that tensile stresses develop along open pore walls and within grain bodies, with the magnitude of these stresses increasing with increasing porosity (Figures 2, 3, and 4a). Though the highest tensile stresses occur at the open pore wall surfaces closest to grain contact edges, substantial tensile stresses develop well outside the contact area as well, that is, on the open pore wall, in all investigated configurations. On inclined contacts undergoing shear during triaxial compression, the largest tensile stress is observed at the leading edge of the contact of the overriding grain (Figures 2a–2c), where its magnitude is enhanced compared to the largest tensile stresses at purely normally loaded contacts (compare Figures 2c and 2d). The substantial tensile stress development well outside the contact area, and the stress enhancement caused by shear stress, are both qualitatively similar to those for Hertzian contacts subjected to normal and tangential loadings with partial sliding (Chiang & Evans, 1983; Hamilton, 1983; Shah & Wong, 1997).

The magnitude of such tensile stresses along grain surfaces (pore walls) outside the contact will impact the probability that a surface flaw of a given size is able to extend. Therefore, we will assess the initiation of critical crack growth using LEFM theory. Based on the similarity between our model and Hertzian contact theory in terms of tensile stress development, we assume that the observed stress field will drive mode I brittle fracturing of the
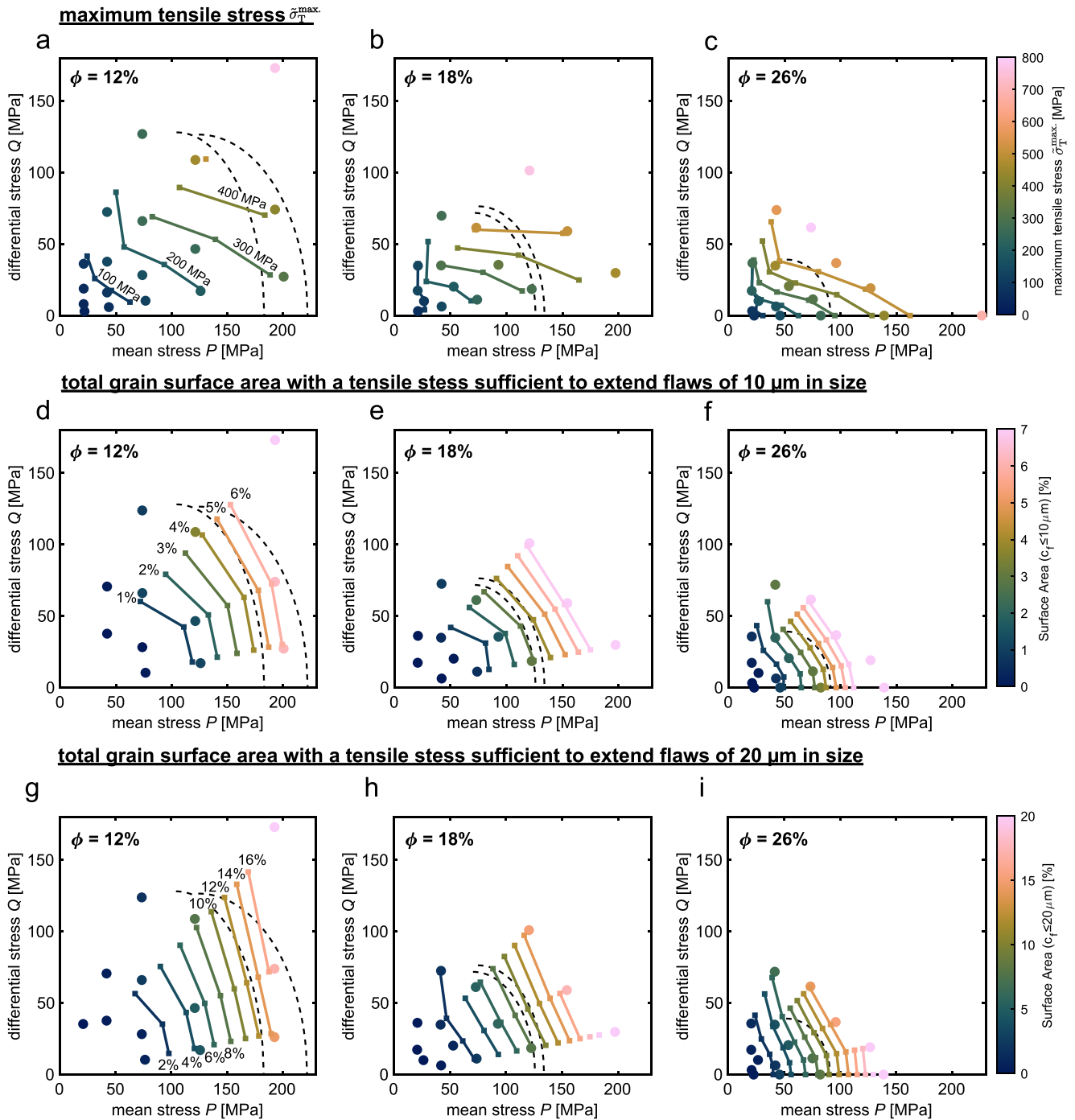
Figure 5. (a–c) Plots showing maximum tensile stress in differential stress (Q) versus mean stress (P) space for simulated grain clusters with (a) $\phi = 12\%$, (b) $\phi = 18\%$ and (c) $\phi = 26\%$. The solid lines delineate contours of equal maximum tensile stress. (d–i) Similar P–Q plots showing the percentage of grain surface area for which the predicted tensile stress is sufficient to extend a given flaw size of (d–f) 10 μm and (g–i) 20 μm in size. Data is presented for (d, g) $\phi = 12\%$, (e, h) $\phi = 18\%$ and (f, i) $\phi = 26\%$. The solid lines indicate contours of equal surface area. Compactive yield envelopes obtained for Slochteren sandstone with similar porosities are shown using dashed black lines (Pijnenburg et al., 2019a).

quartz and feldspar grains, as is often assumed in grain crushing models combining Hertzian contact and LEFM theories (e.g., Zhang et al., 1990). This requires the assumption that a number of sufficiently small (i.e., ≪R), randomly-oriented Griffith-type surface flaws are distributed over the free grain surface. In addition, we assume favorably-oriented flaws (i.e., normal to the minimum principal stress $\tilde{\sigma}_3$ direction) can be considered to be

subjected to a tensile stress σ_T applied perpendicular to the flaw at any location along the grain surface. Surface stress components oriented parallel to the flaw are assumed not to change the tensile stress at the crack tip. Then, the crack tip stress is characterized by the mode I stress intensity factor $K_I = Y\sigma_T\sqrt{\pi c}$, where Y is a dimensionless correction factor to account for crack geometry, loading conditions and edge effects (Lawn, 1993). In terms of LEFM, crack extension occurs when K_I attains a critical value equal to the mode I fracture toughness K_{IC}. At this point, the flaw size c is equal to the critical flaw size c_f. From LEFM theory it is then clear that a doubling in tensile stress at the crack tip, such as resulting from heterogeneity in local porosity (Figure 3a vs. Figure 3d, or Figure 3c vs. Figure 3e), decreases the minimum critical flaw size by a factor of 4. By contrast, in a quartz-feldspar grain contact, the minimum critical flaw size in the quartz grain increases by 16%–33% compared to a quartz-quartz contact (cf. min. $\tilde{\sigma}_3$ for cb29–0.3 vs. cb29-0.3-fsp, and cb12-0.3 vs. cb12-0.3-fsp; Table 2).

To make meaningful inferences for highly porous reservoir sandstones, we apply our numerical results to compaction data obtained for the Slochteren sandstone reservoir in the Groningen Gas Field (Pijnenburg et al., 2019a). To do so, we attempt to quantify the size of a surface flaw that is able to extend (i.e., $c \geq c_f$) in the load-bearing grains of Slochteren sandstone. Following for example, Brzesowsky et al. (2014), we assume that a crack of dimension c_f will remain unstable along its advancement path, causing instantaneous/catastrophic grain failure. The Slochteren sandstone formation is the principal gas-bearing reservoir rock, at roughly 3 km depth with a thickness of 100–250 m (Jager & Visser, 2017). Consisting primarily of aeolian, alluvial, and fan deposits (Jager & Visser, 2017), the reservoir has a variable porosity with mean values of 12%–16% on the fringes and 18%–22% in the center. Furthermore, it contains localized pockets with porosities of up to 26% (NAM, 2013). The Slochteren sandstone consists of quartz (72–90 vol%), with lesser amounts of feldspar (8–25 vol%), clay (0.5–5.5 vol%) and lithic fragments (3–10 vol%) (Waldmann et al., 2014; Waldmann & Gaupp, 2016). The mean size of the quartz and feldspar grains typically ranges between 150 and 250 μm (Pijnenburg et al., 2018). From visual inspection it is clear that the grains have pre-existing surface flaws up to several tens of micrometers in size (e.g., Figure 9a of Pijnenburg et al. (2019a), Figure 2c of Pijnenburg and Spiers (2020)). Clay films (1 to 10 μm thick) coat the quartz and feldspar grain surfaces and many grain contacts (Gaupp et al., 1993; Waldmann & Gaupp, 2016; Wilson, 1992). Overall, Slochteren sandstone has a microstructure (porosity, mineralogy and grain size) which is comparable to the model clusters presented in this study.

Maximum tensile stress $\left(\sigma_T^{max.}\right)$ magnitude and the total grain surface area experiencing a tensile stress sufficient to extend flaw sizes equal to 10 μm (i.e., $c_f \leq 10$ μm) and 20 μm (i.e., $c_f \leq 20$ μm) are plotted in P–Q space for aggregate porosities of 12%, 18% and 26% (Figure 5). The c_f distribution, used to construct the tensile area, was calculated using the tensile stress distribution along the surface of single grains through the following relationship $K_{IC} = Y\sigma_T\sqrt{\pi c_f}$. K_{IC} was taken as equal to 1.0 MPa m$^{1/2}$, a representative value based on double torsion tests performed on synthetic quartz single crystals at room temperature and under ambient dry or wet conditions (Atkinson, 1979; Atkinson & Meredith, 1987), and $Y = 1.12$ (e.g., Brzesowsky et al., 2011; Brzesowsky et al., 2014). Superimposed onto the maximum tensile stress and tensile area contours are the compactive yield envelopes fitted to experimental data obtained for Slochteren sandstone (Pijnenburg et al., 2019a). The yield envelope for sandstones is typically described using the relation

$$\frac{\left(\frac{P}{P^*} - \gamma\right)^2}{(1 - \gamma)^2} + \frac{\left(\frac{Q}{P^*}\right)^2}{\delta^2} = 1, \tag{1}$$

where γ and δ correspond to dimensionless parameters with values ranging from 0 to 1 (Wong et al., 1997), and P^* is the hydrostatic grain crushing pressure. Best fits to the onset point of inelastic compaction C^* data obtained for Slochteren sandstone (Pijnenburg et al., 2019a) gave $(\gamma, \delta, P^*) = (0.56, 0.57, 105)$ and $(\gamma, \delta, P^*) = (0.57, 0.43, 91)$ for $\phi = 21.5\%$ and 26.4%, respectively. Extrapolation of the limited data obtained for $\phi = 13.4\%$ gave two sets of the parameters $(\gamma, \delta, P^*) = (0.56, 0.57, 197)$ and $(\gamma, \delta, P^*) = (0.57, 0.70, 167)$ (see Figures S5a–S5c in Supporting Information S1 for details). Based on the P^*-values obtained in the experiments by Pijnenburg et al. (2019a), estimates for the values of P^* were obtained for $\phi = 12.0\%$, 18.0% and 26.0% (see Figure S5d in Supporting Information S1). This resulted in $P^* = 183$–222, 126–134, and 91 MPa for $\phi = 12.0\%$, 18.0% and 26.0%, respectively. Values of γ and δ for $\phi = 12.0\%$, 18.0% and 26.0% were employed from those for $\phi = 13.4\%$, 21.5% and 26.4%, respectively, assuming the shape of the envelopes remains the same with such little variation in porosity.
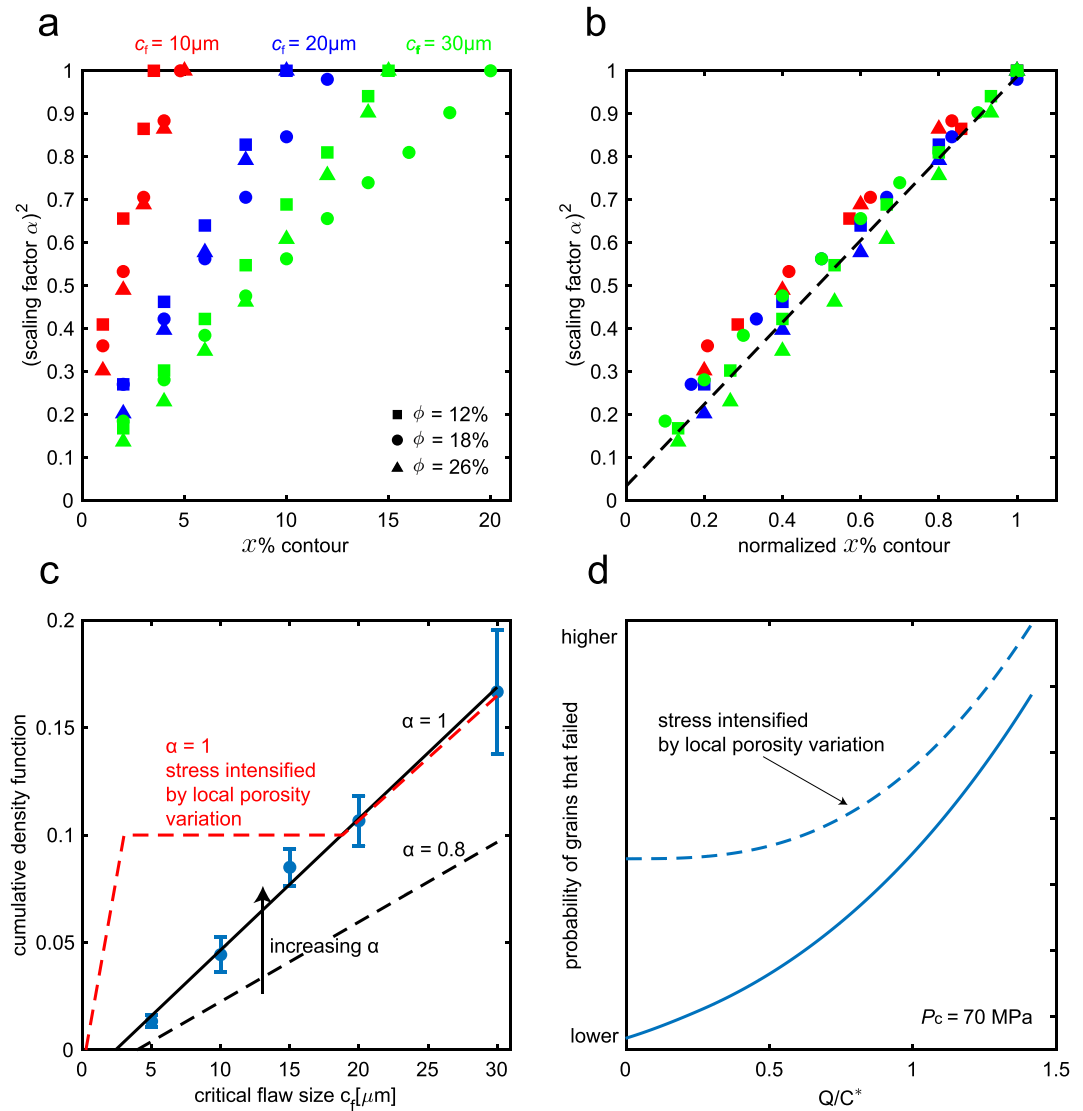
Figure 6. (a) Scaling factor α (see Equation 2 for details) for the ellipse describing a specific tensile area contour (Figure 5), related to the extension of a given flaw size for a given aggregate porosity. (b) Scaling factor as a function of normalized tensile area. Tensile area was normalized with respect to the value for $\alpha = 1$ (i.e., along the yield envelope). (c) Cumulative frequency distributions for critical flaw size along the grain surface, for $\alpha = 1$ and $\alpha = 0.8$. A case with stress intensification due to local porosity variation ($\alpha = 1$) is also shown. (d) Predicted, qualitative grain failure probability, for an aggregate under a confining pressure of 70 MPa, with and without stress intensification.

As expected, the maximum tensile stress computed from the hx12, hx18 and hx26 series (see Table 2) increases with increasing P and Q for all porosities (Figures 5a–5c). While the compactive yield envelopes fitted for Slochteren sandstone (dashed lines) delineate the conditions at which pervasive grain failure is typically observed (e.g., Wong & Baud, 2012), there appears to be little correlation with the tensile stress contours calculated using the hx12, hx18 and hx26 series (see Table 2), that is, the σ_T contours cross-cut the yield envelopes. On the other hand, the contours delineating equal tensile area do show a clear correlation with the compactive envelopes (Figures 5d–5i), as the tensile area contours run roughly parallel to the indicated yield surfaces. This correlation is observed for the total grain surface area experiencing tensile stresses sufficient to extend flaws of ~ 5 to 30 μm in size (see Figure S6 in Supporting Information S1 for additional data on flaw sizes of 5, 15 and 30 μm). Furthermore, for all investigated aggregate porosities with a given flaw size, for example, for a flaw size of 10 μm (i.e., $c_f \leq 10$ μm), all three yield envelopes coincide with the $\sim 4\%$–6% tensile area contour.

This suggests that, at *P-Q* conditions delineated by compactive yield envelopes (i.e., stress conditions at which sandstone fails in an compactive manner), the tensile stress distributions along the grain surface, at least for a tensile stress range corresponding to critical flaw sizes of ~ 5 to 30 μm in size, are insensitive to porosity. It should be noted that, in this case, the absolute value of the corresponding tensile area contour (e.g., 4%–6% for $c_f \leq 10$ μm; Figures 5d–5f) has no physical meaning. As demonstrated earlier (Figures 3 and 4), variations in mineralogy and grain boundary structure will impact the tensile area, as these variations can act as stress intensifiers or reducers. Nonetheless, our simulations suggest that heterogeneity in local porosity, mineralogy or friction coefficient (i.e., here representing intergranular clay) impacts the tensile area to a similar extent regardless of aggregate porosity. Therefore, we infer that the tensile area contour along the compactive envelope would also be quantitatively similar for all the porosities investigated, for a given flaw size. This correlation between the tensile area contours and the compactive yield envelopes for such a wide range of porosities (i.e., 12% and 26%) is remarkable, although we are not yet able to explain the reason for the correlation on a quantitative basis. More work is needed to clarify the underlying reasons for the correlation and to validate and calibrate our model against compaction data for other sandstones besides the Slochteren material.

If we assume that mineralogy, grain boundary structure and flaw size population are independent of aggregate porosity, then this correlation would suggest that the failure of porous sandstones in the compactive regime, such as is the case for the Slochteren sandstone, is related to the probability of pre-existing flaws with a size of up to ~ 30 μm, located in a portion of the grain surface outside of the contact area experiencing sufficiently high tensile stress. This differs from conventional Hertzian-type grain failure, which always initiates from the edge of the grain contact. Surface flaws of grains are known to be generated due to grain collision and abrasion during sedimentary transport (e.g., Mazzullo et al., 1986). Therefore, a single surface flaw population is believed to be a reasonable assumption for sandstone with similar grain size and composition, sampled from the same sedimentary environment. Furthermore, the assumption that mineralogy does not have a direct correlation with porosity for the Slochteren sandstone seems to be reasonable since no qualitative correlation is found between porosity and mineralogy (NAM, 2017). It should be noted though that in our simulations we assumed flat grain contacts. However, it is perfectly possible that grain roughness, that is, asperities within the grain contact, may impact stress distribution and grain failure (Brzesowsky et al., 2011), and that this may lead to crack propagation from within the grain contact, due to stress intensification at asperities or voids.

5. Toward a Probability Model for Crack Growth in Porous Sandstones

We have shown above that the contours delineating areas of equal tensile stress range on grain surfaces qualitatively correlate with the compactive envelopes for Slochteren sandstone, assuming critical flaw sizes at grain surfaces in the range ~ 5 to 30 μm (Figures 5d–5i). As such, the tensile area contours can be described by an equation similar in form to a yield envelope (cf. Equation 1),

$$\frac{\left(\frac{P}{P^*} - \alpha\gamma\right)^2}{(1-\gamma)^2} + \frac{\left(\frac{Q}{P^*}\right)^2}{\delta^2} = \alpha^2, \tag{2}$$

where α is a scaling factor with a value of between 0 and 1. The values of α for area contours representing critical flaw sizes equal to or smaller than 10 to 30 μm are presented in Figure 6a. Here, again, $(\gamma, \delta, P^*) = (0.57, 0.70, 183)$, $(\gamma, \delta, P^*) = (0.56, 0.57, 130)$ and $(\gamma, \delta, P^*) = (0.57, 0.43, 91)$ were employed for $\phi = 12.0$, 18.0% and 26.0%, respectively (see Figure S5 in Supporting Information S1). The values of α^2 showed a linear relationship versus the percentage x of the tensile area mapped for each critical flaw size and porosity (Figure 6a), allowing this relationship to be approximated by a single, universal straight line, whereby the tensile area is normalized with respect to the tensile area at $\alpha = 1$ (i.e., yielding the area percentage aligning with the compactive envelope) (Figure 6b). By using this linear relation and the value of the tensile area contour at $\alpha = 1$, cumulative density functions for the critical flaw size distribution $F(c_f)$ are obtained at α from 0 to 1 (for the case of $\alpha = 0.8$ and 1, see Figure 6c). Using this c_f distribution, combined with Equation 2, enables us to reconstruct critical flaw size (i.e., tensile area) distributions as a function of *P* and *Q*. To calculate the probability of a grain failing, the surface flaw size distribution (i.e., surface flaw density ρ as a function of flaw size c; $\rho(c)$) must be known. If we assume a typical surface flaw intersects a grain surface, defining a half-elliptical shape, then the grain surface area that flaws of a given size take up, relative to the total surface area of a grain, is expressed as

$A/A_0 = g(c) = (a/b)\pi\rho c^2$, where a and b are the short and long axes of the elliptical flaw. Further assuming a uniform orientation distribution of flaws in the grain surface at all points, the probability of a grain failing (p) is directly related to the total surface area occupied by flaws of size c and the probability that these flaws fall in a tensile area where $c_f \leq c$. Hence $p = \int_{c_{min.}}^{c_{max.}} F(x)g(x)h(x)\, dx$, where $h(x)$ is a function taking into account the surface flaw orientation with respect to the tensile stress (i.e., $-\sigma_3$). For sandstone, consisting of many sand grains, this grain failure probability can then be considered to be the percentage of grains failing under a certain state of compression, specified by P and Q.

The grain failure probability was calculated for triaxial compression at a confining pressure of 70 MPa for a porosity of 26%. Note that we have not attempted to introduce a quantitative description of crack length distribution, since such data is not available to the best of the authors' knowledge. This means that our analysis of grain failure probability is only qualitative. Based on our FEM results exploring the effect of local porosity variations, the magnitude of the tensile stress increases by a factor up to 2–3 (Figure 4b) for the top 10% of the tensile stress population. Including this stress intensification (see red dashed curve in Figure 6c), we can estimate the probability of grain failure in aggregates with and without porosity variation. Without stress intensification, the probability of grain failure increases as soon as differential stress is applied, with more rapid increase in the probability with increasing differential stress (Figure 6d). By contrast, when stress intensification is included, little increase in the grain failure probability was observed when $Q/C^* < 0.6$–0.7, followed by a non-linear increase in the probability with increasing Q (Figure 6d). Essentially, stress intensification resulting from porosity or mineralogical variations led to an increase in the probability of grain breakage before the deviatoric loading started, that is, during hydrostatic loading (see increased probability of grains that failed with stress intensification at $Q/C^* = 0$ in Figure 6d). The non-intensified tensile stress is not high enough to increase the probability of breakage significantly at $Q/C^* < 0.6$–0.7. When $Q/C^* > 0.6$–0.7, the non-intensified tensile stresses became large enough to initiate extension of larger flaws with sizes up to ~ 30 μm, and extension of smaller flaws as stress further increases.

Though our probability estimates are not fully quantitative, we can qualitatively compare our predicted trends with experimental data. Acoustic emissions are considered to be a good indirect measurement of grain breakage (Carbillet et al., 2021, 2022; Fortin et al., 2009). Let us now compare our probability estimates with existing AE data obtained during triaxial compression experiments at a confining pressure of 70 MPa on Bleurswiller sandstone (Fortin et al., 2009), and on a synthetic sample with a comparable grain geometry, grain size distribution and porosity to our model, deformed in the compactive regime (Carbillet et al., 2021). This shows there is at least qualitative consistency between our predictions and observations in laboratory, notably for the grain failure probability that takes stress intensification into account. Typically in experiments, little to no AEs are detected until a certain threshold stress is overcome, as is also suggested by our probability estimate. However, it should be noted that the predicted probability significantly depends on the selected or assigned surface flaw size distribution and flaw shape. This means that quantitative comparison between the predictions and experimental results is meaningless. Those parameters need to be better constrained before our conceptual model can be used in more meaningful way.

Beyond that, any future developments of our conceptual model should eventually include extending the model to take into account subcritical crack growth. Subcritical crack growth due to stress corrosion cracking is one of the possible mechanisms responsible for time-dependent compaction of porous sandstone (Brantut et al., 2013, 2014; Heap et al., 2009a, 2009b, 2015; Pijnenburg et al., 2018). Hence quantifying the contribution of slow crack growth to time-dependent compaction of porous sandstone reservoir is key to evaluate the impact of fluid extraction.

It should be noted that our conceptual, or future, grain failure probability model assumes homogeneous external stress (i.e., σ_1, σ_2 and σ_3) distribution within sandstone, which may underestimate tensile stress at locally lower porosity regions and overestimate tensile stress at locally higher porosity regions, compared with uniform strain boundary conditions. This will impact the tensile stress distribution at the aggregate scale. In addition, the model does not include other deformation mechanism(s) (e.g., intergranular sliding and intergranular clay film shearing and compaction) which may contribute to compaction. Those mechanisms produce (local) strains leading to stress reduction, which in turn will impact the tensile stress magnitude. Lastly, if stress concentrations caused by grain roughness are present in grain contacts, cracks can emanate from within grain contacts (Pijnenburg et al., 2019a; Pijnenburg & Spiers, 2020). In this case, another law describing such cracking may also need to be incorporated. A model encompassing all relevant mechanisms, and with more appropriate boundary conditions, would be needed in the future to predict the long-term impact of fluid extraction, in particular, in the context of the Groningen Gas Field.

6. Conclusions

In this study, we quantified grain contact and grain body tensile stress fields driving critical crack growth in simulated sandstone. This was done by performing high-resolution 3D linear elastic FEM simulations on simplified grain assemblies. Systematic investigation was conducted on the effect of aggregate porosity, local porosity variation, stress boundary condition and mineralogy (quartz, feldspar, intergranular clay) on grain volume and contact stresses. We concluded the following points:

1. In all simulations, zones of tensile stresses (i.e., $\tilde{\sigma}_3 < 0$) can be observed not just at the edge of the grain contact, but also along substantial sections of the pore wall and within the grain bodies. The magnitude of the tensile stress increases with increasing porosity.
2. Locally replacing a quartz grain by a feldspar (i.e., albite) grain, and changing the friction coefficient to simulate the presence or absence of a clay film, do not show significant effect on tensile stress magnitude (9%–18% reduction and change <1.4%, respectively).
3. By contrast, local porosity variations intensify the magnitude of the tensile stress by a factor of up to 2–3 for the top 10% of the tensile stress population, while simultaneously the majority of the tensile stress population is reduced in magnitude by up to 20%–25%.
4. We made an attempt to quantify the size of surface flaws that can be expected to extend by equilibrium crack growth under the stress conditions of the depleted Groningen gas reservoir sandstone. This was done by comparing compactive yield envelopes of the sandstone with maximum tensile stress and amount of surface area with tensile stresses sufficient to extend flaw with certain sizes. Those comparisons indicated that there appears to be little correlation between the compactive envelopes and the maximum tensile area contours. By contrast, the contours delineating equal tensile area showed a clear correlation with the compactive envelopes. This correlation is observed for the total grain surface area experiencing tensile stresses sufficient to extend flaw sizes of 5 to 30 µm. It suggests that the failure of porous sandstones in the compactive regime, as is the case for the Groningen (Slochteren) sandstone, is related to the probability of pre-existing flaws with a size of up to ∼30 µm falling in a portion of the grain surface outside of the contact area experiencing sufficiently high tensile stress. This is different from conventional Hertzian-type grain failure, which always initiates from the edge of the grain contact.
5. A new route is identified to develop a probability-type model to predict evolution of critical and subcritical crack growth during sandstone compaction. With tensile stress intensification due to local porosity variations, the developed model qualitatively captures the non-linear increase in the amount of grain breakage due to critical crack growth typically inferred from existing AE data during deviatoric loading. However, model development is still at a very early stage, due to poorly constrained parameters for grain surface flaw size distribution, flaw shape and subcritical crack growth. Incorporating other deformation mechanisms, including grain failure caused by cracks emanating from within grain contacts, and allowing for alternative boundary conditions, may be needed in the future to adequately predict the long-term impact of fluid extraction, in particular, in the context of the Groningen Gas Field.

Data Availability Statement

The 3D FEM data, an in-house python code for 2D FEM simulations performed to obtain polynomial functions employed to describe appropriate boundary conditions for some of the 3D simulations, the 2D FEM data and a MATLAB script for the failure probability model are published open access in Shinohara et al. (2024).

References

Atkinson, B. K. (1979). A fracture mechanics study of subcritical tensile cracking of quartz in wet environments. *Pure and Applied Geophysics*, *117*(5), 1011–1024. https://doi.org/10.1007/bf00876082

Atkinson, B. K., & Meredith, P. G. (1987). Experimental fracture mechanics data for rocks and minerals. In B. K. Atkinson (Ed.), *Fracture mechanics of rock* (pp. 477–525). Academic Press.

Baud, P., Reuschlé, T., Ji, Y., Cheung, C. S. N., & Wong, T.-F. (2015). Mechanical compaction and strain localization in Bleurswiller sandstone. *Journal of Geophysical Research: Solid Earth*, *120*(9), 6501–6522. https://doi.org/10.1002/2015jb012192

Bernabé, Y., Fryer, D. T., & Hayes, J. A. (1992). The effect of cement on the strength of granular rocks. *Geophysical Research Letters*, *19*(14), 1511–1514. https://doi.org/10.1029/92gl01288

Bernabé, Y., Fryer, D. T., & Shively, R. M. (1994). Experimental observations of the elastic and inelastic behaviour of porous sandstones. *Geophysical Journal International*, *117*(2), 403–418. https://doi.org/10.1111/j.1365-246x.1994.tb03940.x

Bourne, S. J., & Oates, S. J. (2020). Stress-dependent magnitudes of induced earthquakes in the Groningen gas field. *Journal of Geophysical Research: Solid Earth*, *125*(11), e2020JB020013. https://doi.org/10.1029/2020jb020013

Brantut, N., Heap, M. J., Baud, P., & Meredith, P. G. (2014). Rate- and strain-dependent brittle deformation of rocks. *Journal of Geophysical Research: Solid Earth*, *119*(3), 1818–1836. https://doi.org/10.1002/2013jb010448

Brantut, N., Heap, M. J., Meredith, P. G., & Baud, P. (2013). Time-dependent cracking and brittle creep in crustal rocks: A review. *Journal of Structural Geology*, *52*, 17–43. https://doi.org/10.1016/j.jsg.2013.03.007

Brown, J. M., Angel, R. J., & Ross, N. L. (2016). Elasticity of plagioclase feldspars. *Journal of Geophysical Research: Solid Earth*, *121*(2), 663–675. https://doi.org/10.1002/2015jb012736

Brzesowsky, R. H., Spiers, C. J., Peach, C. J., & Hangx, S. J. T. (2011). Failure behavior of single sand grains: Theory versus experiment. *Journal of Geophysical Research*, *116*(B6), B06205. https://doi.org/10.1029/2010jb008120

Brzesowsky, R. H., Spiers, C. J., Peach, C. J., & Hangx, S. J. T. (2014). Time-independent compaction behavior of quartz sands. *Journal of Geophysical Research: Solid Earth*, *119*(2), 936–956. https://doi.org/10.1002/2013jb010444

Carbillet, L., Heap, M. J., Baud, P., Wadsworth, F. B., & Reuschle, T. (2021). Mechanical compaction of crustal analogs made of sintered glass beads: The influence of porosity and grain size. *Journal of Geophysical Research: Solid Earth*, *126*(4), e2020JB021321. https://doi.org/10.1029/2020jb021321

Carbillet, L., Heap, M. J., Baud, P., Wadsworth, F. B., & Reuschlé, T. (2022). The influence of grain size distribution on mechanical compaction and compaction localization in porous rocks. *Journal of Geophysical Research: Solid Earth*, *127*(11), e2022JB025216. https://doi.org/10.1029/2022jb025216

Chester, F. M. (1994). Effects of temperature on friction: Constitutive equations and experiments with quartz gouge. *Journal of Geophysical Research*, *99*(B4), 7247–7261. https://doi.org/10.1029/93jb03110

Chiang, S.-S., & Evans, A. G. (1983). Influence of a tangential force on the fracture of two contacting elastic bodies. *Journal of the American Ceramic Society*, *66*(1), 4–10. https://doi.org/10.1111/j.1151-2916.1983.tb09957.x

Davies, R., Foulger, G., Bindley, A., & Styles, P. (2013). Induced seismicity and hydraulic fracturing for the recovery of hydrocarbons. *Marine and Petroleum Geology*, *45*, 171–185. https://doi.org/10.1016/j.marpetgeo.2013.03.016

De Jager, J., & Visser, C. (2017). Geology of the Groningen field—An overview. *Netherlands Journal of Geosciences*, *96*(5), s3–s15. https://doi.org/10.1017/njg.2017.22

Dempsey, D., & Suckale, J. (2017). Physics-based forecasting of induced seismicity at Groningen gas field, the Netherlands. *Geophysical Research Letters*, *44*(15), 7773–7782. https://doi.org/10.1002/2017gl073878

De Waal, J. A., & Smits, R. M. M. (1988). Prediction of reservoir compaction and surface subsidence: Field application of a new model. *SPE Formation Evaluation*, *3*(2), 347–356. https://doi.org/10.2118/14214-pa

Eberhart-Phillips, D., & Oppenheimer, D. H. (1984). Induced seismicity in The Geysers Geothermal Area, California. *Journal of Geophysical Research*, *89*(B2), 1191–1207. https://doi.org/10.1029/jb089ib02p01191

Fialko, Y., & Simons, M. (2000). Deformation and seismicity in the Coso geothermal area, Inyo County, California: Observations and modeling using satellite radar interferometry. *Journal of Geophysical Research*, *105*(B9), 21781–21793. https://doi.org/10.1029/2000jb900169

Fortin, J., Stanchits, S., Dresen, G., & Gueguen, Y. (2009). Acoustic emissions monitoring during inelastic deformation of porous sandstone: Comparison of three modes of deformation. *Pure and Applied Geophysics*, *166*, 823–841. https://doi.org/10.1007/978-3-0346-0122-1_5

Gaupp, R., Matter, A., Platt, J., Ramseyer, K., & Walzebuck, J. (1993). Diagenesis and fluid evolution of deeply buried Permian (Rotliegende) gas reservoirs, Northwest Germany. *AAPG Bulletin*, *77*(7), 1111–1128. https://doi.org/10.1306/bdff8e0c-1718-11d7-8645000102c1865d

Guéguen, Y., & Fortin, J. (2013). Elastic envelopes of porous sandstones. *Geophysical Research Letters*, *40*(14), 3550–3555. https://doi.org/10.1002/grl.50676

Hamilton, G. (1983). Explicit equations for the stresses beneath a sliding spherical contact. *Proceedings of the Institution of Mechanical Engineers–Part C: Journal of Mechanical Engineering Science*, *197*(1), 53–59. https://doi.org/10.1243/pime_proc_1983_197_076_02

Heap, M. J., Baud, P., & Meredith, P. G. (2009). Influence of temperature on brittle creep in sandstones. *Geophysical Research Letters*, *36*(19), L19305. https://doi.org/10.1029/2009gl039373

Heap, M. J., Baud, P., Meredith, P. G., Bell, A. F., & Main, I. G. (2009). Time-dependent brittle creep in Darley dale sandstone. *Journal of Geophysical Research*, *114*(B7), B07203. https://doi.org/10.1029/2008jb006212

Heap, M. J., Brantut, N., Baud, P., & Meredith, P. G. (2015). Time-dependent compaction band formation in sandstone. *Journal of Geophysical Research: Solid Earth*, *120*(7), 4808–4830. https://doi.org/10.1002/2015jb012022

Hertz, H. (1881). The contact of elastic solids. *J Reine und Angewandte Mathematik*, *92*, 156–171.

Hettema, M., Papamichos, E., & Schutjens, P. M. T. M. (2002). Subsidence delay: Field observations and analysis. *Oil and Gas Science and Technology*, *57*(5), 443–458. https://doi.org/10.2516/ogst:2002029

Hiramatsu, Y., & Oka, Y. (1966). Determination of the tensile strength of rock by a compression test of an irregular test piece. *International Journal of Rock Mechanics and Mining Sciences and Geomechanics Abstracts*, *3*(2), 89–99. https://doi.org/10.1016/0148-9062(66)90002-7

Hol, S., Mossop, A. P., Van der Linden, A. J., Zuiderwijk, P. M. M., & Makurat, A. H. (2015). Long-term compaction behavior of Permian sandstones–An investigation into the mechanisms of subsidence in the Dutch Wadden Sea. In *49th US rock mechanics/geomechanics symposium*.

Hol, S., Van der Linden, A. J., Bierman, S., Marcelis, F., & Makurat, A. H. (2018). Rock physical controls on production-induced compaction in the Groningen field. *Scientific Reports*, *8*(1), 1–13. https://doi.org/10.1038/s41598-018-25455-z

Hurley, R. C., Hall, S. A., Andrade, J. E., & Wright, J. (2016). Quantifying interparticle forces and heterogeneity in 3D granular materials. *Physical Review Letters*, *117*(9), 098005. https://doi.org/10.1103/physrevlett.117.098005

Hurley, R. C., Lind, J., Pagan, D. C., Akin, M. C., & Herbold, E. B. (2018). In situ grain fracture mechanics during uniaxial compaction of granular solids. *Journal of the Mechanics and Physics of Solids*, *112*, 273–290. https://doi.org/10.1016/j.jmps.2017.12.007

Imseeh, W. H., & Alshibli, K. A. (2018). 3D finite element modelling of force transmission and particle fracture of sand. *Computers and Geotechnics*, *94*, 184–195. https://doi.org/10.1016/j.compgeo.2017.09.008

Klein, E., Baud, P., Reuschlé, T., & Wong, T.-F. (2001). Mechanical behaviour and failure mode of Bentheim sandstone under triaxial compression. *Physics and Chemistry of the Earth–Part A: Solid Earth and Geodesy*, *26*(1–2), 21–25. https://doi.org/10.1016/s1464-1895(01)00017-5

Lawn, B. R. (1993). *Fracture of brittle solids* (2nd Ed.). Cambridge University Press.

Mallman, E. P., & Zoback, M. D. (2007). Subsidence in the Louisiana coastal zone due to hydrocarbon production. *Journal of Coastal Research*, *50*(SI), 443–448. https://doi.org/10.2112/jcr-si50-085.1

Mazzullo, J., Sims, D., & Cunningham, D. (1986). The effects of eolian sorting and abrasion upon the shapes of fine quartz sand grains. *Journal of Sedimentary Research*, *56*(1), 45–56. https://doi.org/10.1306/212F887D-2B24-11D7-8648000102C1865D

McBride, E. F. (1989). Quartz cement in sandstones: A review. *Earth-Science Reviews*, *26*(1–3), 69–112. https://doi.org/10.1016/0012-8252(89)90019-6

Ministry of Economic Affairs and Climate Policy. (2024). Wet sluiting groningenveld gaat per 19 April 2024 in. Retrieved from https://www.rijksoverheid.nl/onderwerpen/gaswinning-in-groningen/nieuws/2024/04/18/wet-sluiting-groningenveld-gaat-per-19-april-in

Morton, R. A., Purcell, N. A., & Peterson, R. (2001). Field evidence of subsidence and faulting induced by hydrocarbon production in coastal Southeast Texas. *Gulf Coast Association of Geological Societies Transactions*, *51*, 239–248.

Mossop, A., & Segall, P. (1997). Subsidence at the Geysers Geothermal Field, N. California from a comparison of GPS and leveling surveys. *Geophysical Research Letters*, *24*(14), 1839–1842. https://doi.org/10.1029/97gl51792

NAM. (2013). A technical addendum to the Winningsplan Groningen 2013 subsidence, induced earthquakes and seismic hazard analysis in the Groningen field. *NAM Report, Assen*.

NAM. (2017). Petrographic study of well Zeerijp-3A (ZRP-3A). *NAM Report, Assen*.

Ngwenya, B. T., Main, I. G., Elphick, S. C., Crawford, B. R., & Smart, B. G. D. (2001). A constitutive law for low-temperature creep of water-saturated sandstones. *Journal of Geophysical Research*, *106*(B10), 21811–21826. https://doi.org/10.1029/2001jb000403

Pijnenburg, R. P. J., & Spiers, C. J. (2020). Microphysics of inelastic deformation in reservoir sandstones from the seismogenic center of the Groningen gas field. *Rock Mechanics and Rock Engineering*, *53*(12), 5301–5328. https://doi.org/10.1007/s00603-020-02215-y

Pijnenburg, R. P. J., Verberne, B. A., Hangx, S. J. T., & Spiers, C. J. (2018). Deformation behavior of sandstones from the seismogenic Groningen gas field: Role of inelastic versus elastic mechanisms. *Journal of Geophysical Research: Solid Earth*, *123*(7), 5532–5558. https://doi.org/10.1029/2018jb015673

Pijnenburg, R. P. J., Verberne, B. A., Hangx, S. J. T., & Spiers, C. J. (2019a). Inelastic deformation of the Slochteren sandstone: Stress-strain relations and implications for induced seismicity in the Groningen gas field. *Journal of Geophysical Research: Solid Earth*, *124*(5), 5254–5282. https://doi.org/10.1029/2019jb017366

Pijnenburg, R. P. J., Verberne, B. A., Hangx, S. J. T., & Spiers, C. J. (2019b). Intergranular clay films control inelastic deformation in the Groningen gas reservoir: Evidence from split-cylinder deformation tests. *Journal of Geophysical Research: Solid Earth*, *124*(12), 12679–12702. https://doi.org/10.1029/2019jb018702

Sackfield, A., & Hills, D. A. (1986). The strength of some non-Hertzian plane contacts. *Journal of Tribology*, *108*(4), 655–658. https://doi.org/10.1115/1.3261296

Santarelli, F. J., Tronvoll, J. T., Svennekjaier, M., Skeie, H., Henriksen, R., & Bratli, R. K. (1998). Reservoir stress path: The depletion and the rebound. In *SPE/ISRM rock mechanics in petroleum engineering*.

Shah, K. R., & Wong, T.-F. (1997). Fracturing at contact surfaces subjected to normal and tangential loads. *International Journal of Rock Mechanics and Mining Sciences*, *34*(5), 727–739. https://doi.org/10.1016/s0148-9062(97)00007-7

Shalev, E., Lyakhovsky, V., Ougier-Simonin, A., Hamiel, Y., & Zhu, W. (2014). Inelastic compaction, dilation and hysteresis of sandstones under hydrostatic conditions. *Geophysical Journal International*, *197*(2), 920–925. https://doi.org/10.1093/gji/ggu052

Shinohara, T., Thieulot, C., Spiers, C. J., & Hangx, S. J. T. (2024). *Data and software used in: "Non-Hertzian stress fields in simulated sandstone grains and implications for compactive brittle failure–A high-resolution FEM approach"*. Yoda data publication platform of Utrecht University. https://doi.org/10.24416/UU01-1YQPU8

Smith, M. (2009). *ABAQUS/Standard user's manual, version 6.9*. Dassault Systèmes Simulia Corp.

Spiers, C. J., Hangx, S. J. T., & Niemeijer, A. R. (2017). New approaches in experimental research on rock and fault behaviour in the Groningen gas field. *Netherlands Journal of Geosciences*, *96*(5), s55–s69. https://doi.org/10.1017/njg.2017.32

Stanchits, S., Fortin, J., Guéguen, Y., & Dresen, G. (2009). Initiation and propagation of compaction bands in dry and wet Bentheim sandstone. *Pure and Applied Geophysics*, *166*(5), 843–868. https://doi.org/10.1007/s00024-009-0478-1

Suckale, J. (2009). Induced seismicity in hydrocarbon fields. In *Advances in geophysics* (Vol. 51, pp. 55–106). Elsevier. https://doi.org/10.1016/s0065-2687(09)05107-3

Turner, A. K., Kim, F. H., Penumadu, D., & Herbold, E. B. (2016). Meso-scale framework for modeling granular material using computed tomography. *Computers and Geotechnics*, *76*, 140–146. https://doi.org/10.1016/j.compgeo.2016.02.019

Van Thienen-Visser, K., & Breunese, J. N. (2015). Induced seismicity of the Groningen gas field: History and recent developments. *The Leading Edge*, *34*(6), 664–671. https://doi.org/10.1190/tle34060664.1

Van Wees, J.-D., Buijze, L., Van Thienen-Visser, K., Nepveu, M., Wassing, B. B. T., Orlic, B., & Fokker, P. A. (2014). Geomechanics response and induced seismicity during gas field depletion in the Netherlands. *Geothermics*, *52*, 206–219. https://doi.org/10.1016/j.geothermics.2014.05.004

Van Wees, J.-D., Osinga, S., Van Thienen-Visser, K., & Fokker, P. A. (2018). Reservoir creep and induced seismicity: Inferences from geo-mechanical modeling of gas depletion in the Groningen field. *Geophysical Journal International*, *212*(3), 1487–1497. https://doi.org/10.1093/gji/ggx452

Verberne, B. A., Hangx, S. J. T., Pijnenburg, R. P., Hamers, M. F., Drury, M. R., & Spiers, C. J. (2021). Drill core from seismically active sandstone gas reservoir yields clues to internal deformation mechanisms. *Geology*, *49*(5), 483–487. https://doi.org/10.1130/g48243.1

Waldmann, S., Busch, A., Van Ojik, K., & Gaupp, R. (2014). Importance of mineral surface areas in Rotliegend sandstones for modeling CO_2–water–rock interactions. *Chemical Geology*, *378*, 89–109. https://doi.org/10.1016/j.chemgeo.2014.03.014

Waldmann, S., & Gaupp, R. (2016). Grain-rimming kaolinite in Permian Rotliegend reservoir rocks. *Sedimentary Geology*, *335*, 17–33. https://doi.org/10.1016/j.sedgeo.2016.01.016

Wang, H. F. (2000). *Theory of linear poroelasticity with applications to geomechanics and hydrogeology*. Princeton university press.

Wilson, M. D. (1992). Inherited grain-rimming clays in sandstones from eolian and shelf environments: Their origin and control on reservoir properties. In D. W. Houseknecht & E. D. Pittman (Eds.), *Origin, diagenesis, and petrophysics of clay minerals in sandstone*, (p. 282). https://doi.org/10.2110/pec.92.47.0209

Wong, T.-F., & Baud, P. (2012). The brittle-ductile transition in porous rock: A review. *Journal of Structural Geology*, *44*, 25–53. https://doi.org/10.1016/j.jsg.2012.07.010

Wong, T.-F., David, C., & Zhu, W. (1997). The transition from brittle faulting to cataclastic flow in porous sandstones: Mechanical deformation. *Journal of Geophysical Research*, *102*(B2), 3009–3025. https://doi.org/10.1029/96jb03281

Wong, T.-F., & Wu, L.-C. (1995). Tensile stress concentration and compressive failure in cemented granular material. *Geophysical Research Letters*, *22*(13), 1649–1652. https://doi.org/10.1029/95gl01596

Zbinden, D., Rinaldi, A. P., Urpi, L., & Wiemer, S. (2017). On the physics-based processes behind production-induced seismicity in natural gas fields. *Journal of Geophysical Research: Solid Earth*, *122*(5), 3792–3812. https://doi.org/10.1002/2017jb014003

Zhai, C., Pagan, D., & Hurley, R. (2020). In situ X-ray tomography and 3D X-ray diffraction measurements of cemented granular materials. *The Journal of the Minerals, Metals & Materials Society*, *72*(1), 18–27. https://doi.org/10.1007/s11837-019-03774-4

Zhang, J., Wong, T.-F., & Davis, D. M. (1990). Micromechanics of pressure-induced grain crushing in porous rocks. *Journal of Geophysical Research*, *95*(B1), 341–352. https://doi.org/10.1029/jb095ib01p00341

References From the Supporting Information

Davis, R., & Selvadurai, A. (1996). *Elasticity and geomechanics*. Cambridge University Press

Geuzaine, C., & Remacle, J.-F. (2009). Gmsh: A 3-D finite element mesh generator with built-in pre-and post-processing facilities. *International Journal for Numerical Methods in Engineering*, *79*(11), 1309–1331. https://doi.org/10.1002/nme.2579

Sadd, M. (2014). *Elasticity. Theory, applications and numerics (third edition)*. Elsevier